Turbulent kinetic energy dissipation rate and associated fluxes in the western tropical Atlantic estimated from ocean glider observations

Peter M.F. Sheehan[1], Gillian M. Damerell[1], Philip J. Leadbitter[1], Karen J. Heywood[1], and Rob A. Hall[1]

[1]Centre for Ocean and Atmospheric Sciences, School of Environmental Science, University of East Anglia, Norwich, NR4 7TJ, United Kingdom

Correspondence: Peter Sheehan (p.sheehan@uea.ac.uk)

Abstract. Ocean gliders enable us to collect the high-resolution microstructure observations necessary to calculate the dissipation rate of turbulent kinetic energy, ε, on timescales of weeks to months: far longer than is normally possible using traditional ship-based platforms. Slocum gliders have previously been used to this end; here, we report the first detailed estimates of ε calculated using the Batchelor spectrum method on observations collected by a FP07 fast thermistor mounted on a Seaglider. We use these same fast thermistor observations to calculate ε following the Thorpe scale method and find very good agreement between the two methods. The Thorpe scale method yields larger values of ε, but the average difference, which is less than an order of magnitude, is smaller than reported elsewhere. The spatio-temporal distribution of ε is comparable for both methods. Maximum values of ε (10^{-7} W kg^{-1}) are observed in the surface mixed layer; values of approximately 10^{-9} W kg^{-1} are observed between approximately 200 and 500 m depth. These two layers are separated by a 100 m thick layer of low ε (10^{-10} W kg^{-1}), which is co-located with a high-salinity layer of Subtropical Underwater and a peak in the strength of stratification. We calculate the turbulent heat and salt fluxes associated with the observed turbulence. Between 200 and 500 m, ε induces downward fluxes of both properties that, if typical of the annual average, would have a very small influence on the heat and salt content of the overlying salinity-maximum layer. We compare these turbulent fluxes with ~~two~~ estimates of double-diffusive fluxes ~~, having objectively identified those regions of the water column where double diffusion is likely to occur~~that occur in regions susceptible to salt fingers, such as the western tropical Atlantic. We find that the double-diffusive fluxes of both heat and salt are larger than the corresponding ~~mechanical~~ turbulent fluxes.

1 Introduction

Turbulence in the ocean, and the mixing of different water masses that it induces, are of fundamental importance to ocean dynamics. Over relatively small scales, turbulent mixing often controls the distribution of key water mass properties and tracers; over the world ocean, the sum of these small-scale processes is responsible for the closure of the thermohaline circulation and for the primary production that relies on the upward flux of nutrients to the euphotic zone.

Estimating the dissipation rate of turbulent kinetic energy, ε, ~~by applying the Batchelor spectrum method (Batchelor, 1959) to~~ from high-resolution observations of shear and temperature ~~(e.g. Lueck et al., 2002; Peterson and Fer, 2014; Scheifele et al., 2018)~~ (e.g. Lueck et al., 2002; Oakey, 1982; Ruddick et al., 2000) has, historically, required considerable ship time, plus specialist
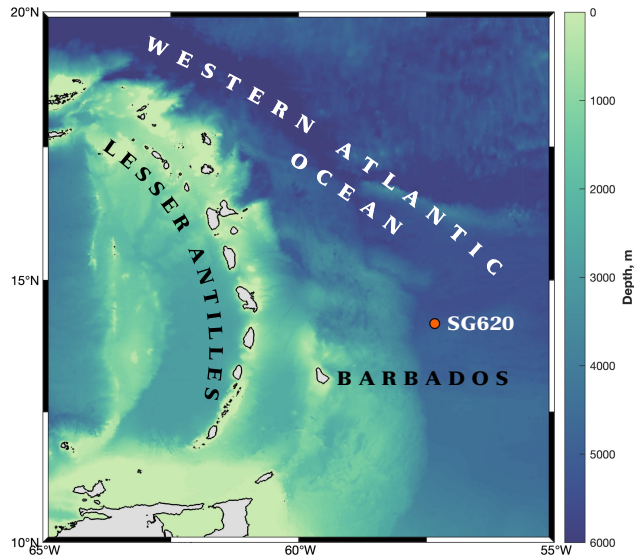
Figure 1. Bathymetry (m) of the western tropical Atlantic and the the eastern Caribbean Sea in the region of the Lesser Antilles. The location of SG620, northeast of Barbados, is marked by the orange circle. Land is shaded grey.

25 instruments and expertise~~. Consequently, spectrum-based estimates having been difficult to acquire,~~, so there are relatively few of ~~them; for instance, Fernández-Castro et al. (2014) collect only 50 profiles of ε from a circumnavigation of the tropics~~such estimates. Methods such as Thorpe scaling (Thorpe, 1977) and ~~fine-scale~~ finescale parameterisation (Polzin et al., 2014; Whalen et al., 2015) have been developed to enable ε to be estimated from ~~ordinary~~ standard CTD and ADCP observations of temperature, salinity and ~~velocity. Yet, although non-spectral~~ current velocity – hereafter referred to as finescale methods and

30 observations. Although finescale methods do not require specialist instruments ~~and may be applied to ordinary oceanographic observations~~ (e.g. Fer et al., 2010b; Whalen et al., 2012, 2015), ~~these methods~~ they are dependent on more assumptions~~, and~~; their results tend not to be valid over as wide a range of conditions as those ~~of spectral methods (Polzin et al., 2014; Whalen, 2021)~~ derived from high-resolution, microstructure-scale observations (Polzin et al., 2014; Whalen, 2021) – hereafter referred to as microstructure methods and observations. Thus, despite the widespread ~~application of the Thorpe scale and fine-scale~~

35 ~~parameterisation~~ use of finescale methods, the potential remains for discrepancies between ~~spectrum- and non-spectrum-based~~ estimates of ε based on finescale and microstructure observations (Howatt et al., 2021).

Given the proliferation in the use of buoyancy-driven ocean gliders over the last decade, there is growing interest in using them to collect ~~the high-resolution microstructure observationsnecessary to estimate ε using spectral methods~~microstructure observations. Because of a glider's smooth flight through the water column, it resembles the free-falling, loosely tethered pro-

40 filers traditionally used to collect microstructure observations. A growing body of literature makes use of microstructure observations collected by gliders, as well as setting out the best ways of processing such data sets (e.g. Fer et al., 2010b; Peterson and Fer, 2014; Palmer et al., 2015; Schultze et al., 2017; Scheifele et al., 2018; Scott et al., 2021). Up until now, the ~~vast~~ majority of

studies have used microstructure shear observations collected by Slocum gliders (Palmer et al., 2015). Some authors have used microstructure temperature observations to estimate ε (e.g. Peterson and Fer, 2014; Scheifele et al., 2018), while Rainville et al. (2017) briefly discuss the microstructure system developed for use on Seagliders, another commonly used glider platform, and present estimates of the rate of dissipation of temperature variance, χ. However, observational studies of turbulence using autonomous platforms other than Slocum gliders are known to be lacking (Frajka-Williams et al., 2021). Here, we report in detail the first microstructure-based estimates of ε calculated from Seaglider microstructure temperature observations, and we compare the results with estimates of ε calculated by applying the Thorpe scale method, commonly applied to finescale temperature and salinity observations, to the same microstructure observations.

The western tropical Atlantic (Fig. 1) is known for the persistent presence of the salt fingering regime of double-diffusion (Schmitt et al., 1987; Rollo et al., 2022). For salt fingering to occur, warm, saline water must overlie cooler, fresher water: the water column is therefore stably stratified by temperature but unstably stratified by salinity. Such conditions are maintained in the western tropical Atlantic by the presence of Subtropical Underwater (SUW) at the base of the mixed layer, a warm, high-salinity water mass common to tropical regions (Schmitt et al., 1987; Fer et al., 2010a). Beneath SUW, temperature and salinity both decrease with depth. In a salt fingering regime, the slow molecular diffusion of salt relative to the fast diffusion of heat leads to the development of salt fingers: narrow, small-scale filaments of alternately upwelling warming water and downwelling cooling water. Over time, double-diffusive convection and salt fingers promote the formation of thermohaline staircases: temperature and salinity profiles characterised by a series of homogeneous mixed layers separated by sharp, narrow gradient layers. Such staircases have previously been observed in the western tropical Atlantic (Schmitt et al., 1987; Rollo et al., 2022). Importantly for studies of ocean mixing, double diffusive convection enables the vertical transport of heat and salt by a mechanism other than the mechanical, turbulent mixing captured by ε.

Bathymetry (m) of the western tropical Atlantic and the the eastern Caribbean Sea in the region of the Lesser Antilles. The location of SG620, northeast of Barbados, is marked by the orange circle.

Here, we use microstructure temperature observations collected by a Seaglider to estimate ε using the Batchelor spectrum method (Sec. 2.2; Batchelor, 1959) and using the Thorpe scale method (Sec. 2.3; Thorpe, 1977), and compare the results (Sec. 3.1). From these estimates of ε, we derive turbulent fluxes of heat and salt through an observed layer of elevated ε (Sec. 3.2), and compare these with heat and salt fluxes driven by salt fingers and double-diffusive mixing (Sec. 3.3). We discuss the results in Sec. 4.

2 Data and methods

2.1 Glider observations

As part of the EUREC4A field campaign (Stevens et al., 2021), Seaglider 620 was deployed at 14.2°N, 57.3°W, approximately 200 km northeast of Barbados (Fig. 1) on 23 January 2020. It completed 131 dives to 750 m before being recovered on 5 February 2020. The glider carried an unpumped CT sail measuring in situ conductivity and temperature, and a microstructure system. Given the shape of the Seaglider's hull, it is not possible to mount an all-in-one microstructure payload, such as the ~~RSI~~ Rockland Scientific International (RSI) MicroRider that is used on Slocum gliders (e.g., Fer et al., 2014; Schultze et al., 2017; Scheifele et al., 2018). Instead, a reconfigured payload is used, one consisting of a pair of RSI MicroPod sensor modules mounted either side of the CT sail, and a dedicated pressure housing containing the system's DataLogger mounted inside the Seaglider's aft fairing (Creed et al., 2015). The system draws its power from the Seaglider and ~~was developed and manufactured by Rockland Scientific International~~ can be turned on and off on a dive-by-dive basis.

During the EUREC4A campaign, the glider was equipped with one MicroPod carrying a shear probe and one MicroPod carrying an FP07 fast-response temperature ~~probe. The FP07 probe~~ sensor. There was a fault with the shear probe on this deployment and the observations could not be used. The fast thermistor sensor samples at 512 Hz and has a sensitivity of better than 0.1 mK (Sommer et al., 2013); thermal inertia of the sensor is such that its effective resolution is estimated to be 10 ms (i.e. 100 Hz; Sommer et al., 2013). Microstructure temperature observations are better suited than shear observations to estimating ε in low-dissipation environments (Scheifele et al., 2018), and have the added advantage of being less readily contaminated by platform vibration (Frajka-Williams et al., 2021); here we focus on the temperature-based estimates of epsilon. The glider's hydrodynamic flight model, which is used to estimate along-path speed, is tuned following Frajka-Williams et al. (2011), and the thermal lag of the standard CT sail is corrected following Garau et al. (2011).

2.2 Estimating ε using ~~spectral methods~~ the Batchelor spectrum method

We estimate ε from the glider's fast thermistor temperature microstructure observations using the Batchelor spectrum method; we hereafter refer to these estimates as ε_μ. For this, we use the Matlab toolbox produced by Benjamin Scheifele and Jeffrey Carpenter (github.com/bscheife/turbulence_temperature) and recently used by Howatt et al. (2021). The method is described in detail by Scheifele et al. (2018), and much of the underlying theory, and a similar methodology, are described by Peterson and Fer (2014), so we here give only an outline.

~~Example of temperature spectra, Ψ, that were accepted (left) and rejected (right) by the quality control algorithm. Observed and theoretical spectra are shown by the thin, light-coloured lines; the second-order polynomial fits are shown by thick, dark-coloured lines.~~

We divide the temperature time series from the ~~FP07~~ fast thermistor into half-overlapping segments of 32 seconds length. Within each 32-second segment, we further divide the measurements into 15 four-second, half-overlapping sub-segments. From each sub-segment, we calculate a temperature power spectrum, Δ_4. We then average these 15 Δ_4 to produce one power spectrum, Δ_{32}, that is representative of the original 32-second segment. Values of Δ_{32} at high frequencies, where the thermal

inertial of the fast thermistor is such that its temporal response is inadequate, are corrected using the transfer function of Sommer et al. (2013). We convert each Δ_{32} from frequency space to wavenumber space (Fig. 2) using the glider's along-path speed averaged over the same 32 seconds, and assuming the validity of Taylor's frozen turbulence hypothesis (Scheifele et al., 2018).

We transform each Δ_{32} into a temperature-gradient spectrum, ~~Ψ~~ $\Psi = (2\pi k)^2 \Delta_{32}$, which should resemble the Batchelor spectrum, Ψ_B (Batchelor, 1959), the theoretical spectrum that describes temperature-gradient spectra and which is commonly used when calculating ε_μ ~~(e.g. Peterson and Fer, 2014; Scheifele et al., 2018)~~ (e.g. Oakey, 1982; Ruddick et al., 2000; Peterson and Fer, 2014; S . The Batchelor spectrum is a function of k_B, the Batchelor wavenumber, and of χ, the rate of destruction of ~~temperature-gradient~~ temperature variance (Osborn and Cox, 1972). A comprehensive mathematical treatment of the use of Ψ_B when estimating ε is given by Peterson and Fer (2014). Here, we require k_B in order to calculate ε_μ (W kg^{-1}) according to:

$$\varepsilon_\mu = \nu D_T^2 (2\pi k_B)^4 \tag{1}$$

where ν is the kinematic viscosity of seawater, $D_T = 1.44 \times 10^{-7}$ m^2 s^{-1} is the molecular diffusion coefficient of temperature.

We calculate χ according to:

$$\begin{aligned} \chi &= \chi_l + \chi_{obs} + \chi_u \\ &= 6D_T \left(\int_0^{k_l} \Psi_B \, dk + \int_{k_l}^{k_u} \Psi \, dk + \int_{k_u}^{\infty} \Psi_B \, dk \right) \end{aligned} \tag{2}$$

where χ_{obs} is that part of χ derived by integrating Ψ, and χ_l and χ_u are correction terms derived from Ψ_B. The factor of six comes from assuming isotropic turbulence. The wavenumbers k_l and k_u are, respectively, the lower and upper wavenumber limits of the range over which Ψ is considered reliable; the criteria for choosing k_l and k_u are explained fully by Scheifele et al. (2018). Given an estimate of χ, the maximum likelihood estimation procedure of Ruddick et al. (2000) is used to find the value of k_B ~~where~~ corresponding to the Ψ_B that is the best fit to Ψ between k_l and k_u. On the first iteration, χ_l and χ_u are set to zero and hence $\chi = \chi_{obs}$. On subsequent iterations, the previous value of χ and the previous best-fit value of k_B are used to estimate Ψ_B and hence χ_l and χ_u, and the estimate of k_B is further refined.

An observed spectrum that deviates from the shape of the relevant theoretical spectrum should not be used to estimate ε_μ. To discriminate between acceptably and unacceptably shaped spectra, we fit second order polynomials of the form:

$$P(k) = a.log_{10}(k)^2 + b.log_{10}(k) + c \tag{3}$$

to both the observed and the theoretical spectra, following the method of Scott et al. (2021), where k is wavenumber and a, b and c are the polynomial coefficients to be determined. Prior to fitting, we normalise each spectrum by dividing by
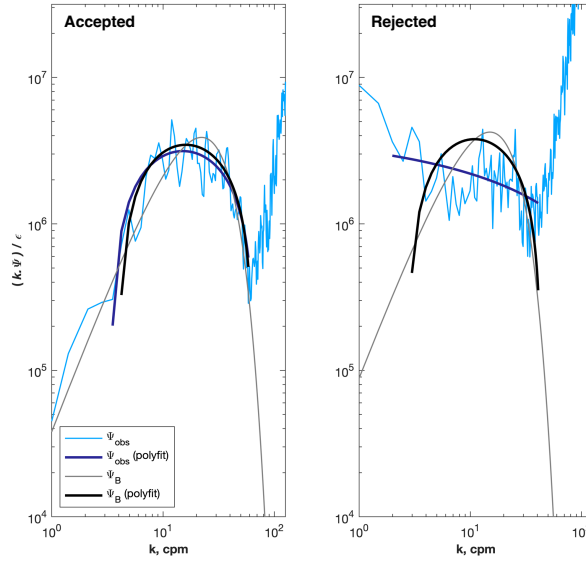
Figure 2. Example of temperature spectra, Ψ, that were accepted (left) and rejected (right) by the quality control algorithm. Observed and theoretical spectra are shown by the thin, light-coloured lines; the second-order polynomial fits are shown by thick, dark-coloured lines.

its corresponding estimate of ε_μ; this enables the same criteria to be used when assessing goodness-of-fit over spectra that otherwise span many orders of magnitude. We also multiply spectra by k in order to preserve variance. P is defined over the

135 same range of wavenumbers over which the observed spectrum is integrated when estimating χ.

We accept a spectrum if:

1. The value of a fitted to Ψ is positive. (Note that a fitted to Ψ_B is always positive.)

2. The ratio of the a values fitted to Ψ_B and Ψ (a_{Ψ_B}/a_Ψ) is less than two.

In addition, following Scheifele et al. (2018), we remove an estimate of ε_μ if:

140 3. Fewer than six points are included in the spectra fit.

4. If the quantity $U/(\varepsilon_\mu/N)^{1/2}$ is less than five, where U is the glider~~'s speed in direction or travel~~'s speed-in-direction-of-travel and $(\varepsilon_\mu/N)^{1/2}$ is an estimate of the turbulent flow velocities (Fer et al., 2014), indicating that ~~Tayor~~'Taylor's frozen turbulence hypothesis is invalid.

5. If the sum of the correction terms χ_u and χ_l is greater than the observed term χ_{obs} (Eqn 2).

145 Finally, following Peterson and Fer (2014), we remove an estimate of ε_μ if:

6. The mean absolute deviation, which quantifies the goodness of fit between Ψ_{obs} and Ψ_B, is greater than $2(2/d)^{1/2}$, where d is the degrees of freedom, calculated as 1.9 multiplied by the number of sub-segments within each 32-second segment, i.e., 1.9×15.

7. The estimate of ε_μ is greater than 2×10^{-7} W kg^{-1}; even having corrected estimates of Δ_{32} at high frequencies, the effective resolution of the fast thermistor (100 Hz) is such that values of ε_μ greater than this cannot be reliably estimated.

~~Time series of hydrographic observations from SG620, averaged into 5 m bins: **(a)** conservative temperature (°C), **(b)** absolute salinity (g kg^{-1}), and **(c)** buoyancy frequency squared (N^2; s^{-2}).~~

Examples of accepted and rejected spectra are presented in Fig. 2. After quality control, 84% of ε_μ estimates remained. Quality-controlled estimates of ε_μ were binned, profile by profile, into 25 m vertical bins; we use the geometric mean ~~(and standard deviation)~~ in preference to the arithmetic (i.e. ordinarily used) mean, the better to represent the average ~~(and spread)~~ of observations that span many orders of magnitude and which are not normally distributed.

2.3 Thorpe scale estimates

We apply the Thorpe scale method (Thorpe, 1977) to the ~~FP07 temperature measurements~~ fast thermistor microstructure potential temperature observations to derive a second, independent estimate of the turbulent kinetic energy dissipation rate, hereafter referred to as ε_T. ~~The sampling frequency of the FP07 thermistor (512 Hz) is faster than its true response time, which Sommer et al. (2013) estimate to be 10 ms (i.e.~~ Given that the effective resolution of the fast thermistor is estimated to be 100 Hz~~). Consequently~~, we apply a low-pass, 12th-order Butterworth filter with a cut-off frequency of 100 Hz to remove the highest-frequency variability. This prevents instrumental noise erroneously manifesting as small density overturns ~~(Mater et al., 2015; ?)~~(Mater et al., 2015; Ijichi and Hibiya, 2018). Temperature observations were then binned ~~(mean-averaged)~~ into 10 ms bins using the arithmetic mean, giving an effective vertical resolution of 3 ± 0.5 mm.

Each temperature profile is then re-ordered in depth so that ~~it is stable in temperature~~temperature always decreases with depth (i.e. is stable with respect to temperature). From the re-ordered profile we calculate the vertical Thorpe displacement, Δz: the difference between an observation's original depth and its re-ordered depth. We identify an overturn as a vertical segment in which the cumulative sum of Δz is non-zero, and which is bounded above and below by segments in which the cumulative sum of Δz is zero. Following ~~?~~Ijichi and Hibiya (2018) and Howatt et al. (2021), we combine all overturns that are smaller than 2 m and are within 1 m of an adjacent overturn until the region is larger than 2 m. Overturns smaller than 2 m that are further than 1 m from an adjacent overturn are not aggregated. This assumes that a succession of small overturns is the signal of a once larger, single overturn that has recently decayed into a series of smaller overturns (Smyth et al., 2001). The Thorpe scale, L_T (~~m~~Fig. 3), is then the root mean square of Δz over an overturn:

$$L_T = \langle \Delta z^2 \rangle^{1/2} \tag{4}$$

where angular brackets indicate the mean. Larger values of L_T correspond to larger mixing rates; the largest values of L_T (approximately 1 m) are found principally between 200 and 500 m, although much lower values (approximately 0.01 m and lower) are also found within this depth range (Fig. 3). Similarly high values of L_T are also found in the bottom 200 m sampled towards the beginning of the deployment. Above 200 m, values of L_T are much lower, being generally below 0.01 m (Fig. 3).
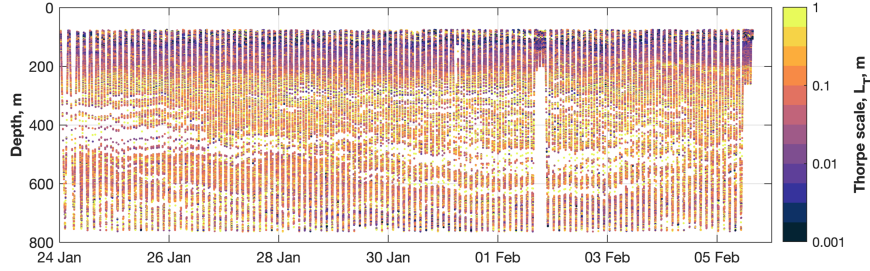
Figure 3. Thorpe scale estimates, L_T (m). Higher values of L_T are indicative of higher dissipation, ε_T.

Finally, we calculate ε_T (W kg^{-1}) from L_T by relating the Ozmidov scale, $L_O = (\varepsilon_T/N^3)^{1/2}$ (Ozmidov, 1965), to ~~the Thorpe scale~~ L_T by the empirical relation $L_O = 0.8\,L_T$ (Dillon, 1982), which yields:

$$\varepsilon_T = 0.64 L_T^2 N^3 \tag{5}$$

where N is the background buoyancy frequency calculated using the Seaglider's finescale temperature and salinity observations~~from the glider's CT sail (binned at~~, binned into 5 m ~~resolution~~vertical bins, then smoothed in the vertical using a Gaussian-windowed running mean over nine bins (i.e. 45 m).

~~We visually inspect~~

Our estimates of ε_T ~~and remove unphysical results: for example regions that exhibit very clear distinctions compared with the surrounding water column, typically characterised by highly elevated values of ε_T. Estimates of ε_T were binned into 25 m bins using the geometric mean.~~~~Temperature is a poor proxy for density in any region of the water column~~ are derived from potential temperature rather than potential density; we must therefore assume that temperature is the dominant control on density. In regions where this is not the case – i.e. in regions where salinity is the dominant control on density~~; consequently, regions of the water column with large salinity variability but little temperature variability can falsely appear to be overturns, or can appear to not contain overturns which are present in reality~~ – temperature perturbations may not correspond to the density perturbations that the Thorpe scale method takes to be indicative of turbulent overturns. To identify ~~such regions~~, ~~we calculate, within each 25 m bin, the ratio, r between the standard deviation of absolute salinity, S, and conservative temperature, Θ~~regions where salinity is the dominant control on density, we use the density ratio, R_ρ:

$$r = \frac{std.dev(S)}{std.dev(\Theta)}$$

$$R_\rho = \frac{\alpha\Theta_z}{\beta S_z} \tag{6}$$

~~Values of r are then normalised: we subtract the mean of r (calculated over the entire data set) and divide by its standard deviation. The mean and standard deviation of $log(r)$ are calculated to limit the influence of bins with extreme values of~~ where α is the thermal expansion co-efficient, Θ_z is the vertical temperature gradient, β is the haline contraction coefficient and S_z is the vertical salinity gradient. We calculate Θ_z and S_z from finescale glider observations binned into 5 m vertical bins using the arithmetic mean, and find R_ρ at the depth of each overturn. Where -1 ~~r. We remove~~ $< R_\rho < 1$, salinity is the dominant control on density, and we discard any overturns and associated value of ε_T. In total, 2388 overturns are discarded by the R_ρ quality control criterion, 4.03% of the total. In the majority of the water column, temperature is the dominant control on density, and so temperature observations may be reliably used to estimate ε. Estimates of ε_T that are discarded correspond principally to large values of L_T (> 1 m) in mid-depth regions (i.e. between 200 and 600 m). This is the part of the water column in which the majority of the thermohaline staircases are found (Rollo et al., 2022).

Finally, we discard all values of ε_T ~~from bins with a normalised r that is greater than or equal to a critical value of 0.5. A range of critical values was investigated; a critical value of 0.5 provided the best compromise between algorithmically removing high values and removing too many data points.~~ shallower than 75 m because a temperature inversion in the mixed layer is erroneously identified as an overturn. Remaining estimates of ε_T are binned into 25 m vertical bins using the geometric mean, as for ε_μ.

3 Results

3.1 Estimates of ε

The water masses observed are typical of the region (e.g. Schmitt et al., 1987). A warm (> 26 °C) surface mixed layer of intermediate salinity overlies SUW, a salinity-maximum (> 37.6 g kg^{-1}) layer located in the upper thermocline (Fig. 4). Beneath SUW, temperature and salinity steadily decrease with depth into the Antarctic Intermediate Water layer that lies beneath (Fig. 4). Two maxima in buoyancy frequency are observed: an upper maximum at the base of the surface isohaline layer, and a lower maximum at the base of the surface isothermal layer (Fig. 4).

~~Turbulent kinetic energy dissipation rate, ε (W kg^{-1}) as estimated using **(a)** the Batchelor spectrum method (ε_μ) and **(b)** the Thorpe scale method (ε_T). The respective means (thick line) and standard deviations (thin lines) are shown in the panels on the right. Note that geometric standard deviation is multiplicative. **(c)** The difference between ε_μ and ε_T.~~

~~Histograms of turbulent kinetic energy dissipation rate as estimated using the Batchelor spectrum method (green line) and the Thorpe scale method (purple line; both W kg^{-1}).~~

There is generally good agreement between ε_μ and ε_T ~~(Figs. 5 and ??.~~ Histograms of the two distributions are very similar and, when scattered one against the other, the points are clustered around the one-to-one line (Fig. 6a and b). The ~~higher of the two is~~ principal difference is at depths between 400 and 600 m in the first two days of the deployment, when ε_μ ($> 10^{-9}$ W kg^{-1}) is noticeably higher than ε_T ~~, as can be seen in the depth-time distributions and mean profiles (~~ ($< 10^{-10}$ W kg^{-1}; Fig. 5)~~, and in the histograms (Fig. ??). The spatio-temporal~~. This is a region with a clear pattern in the differences between ε_μ and ε_T: in many other regions, the differences are fairly randomly distributed (Fig 5c).
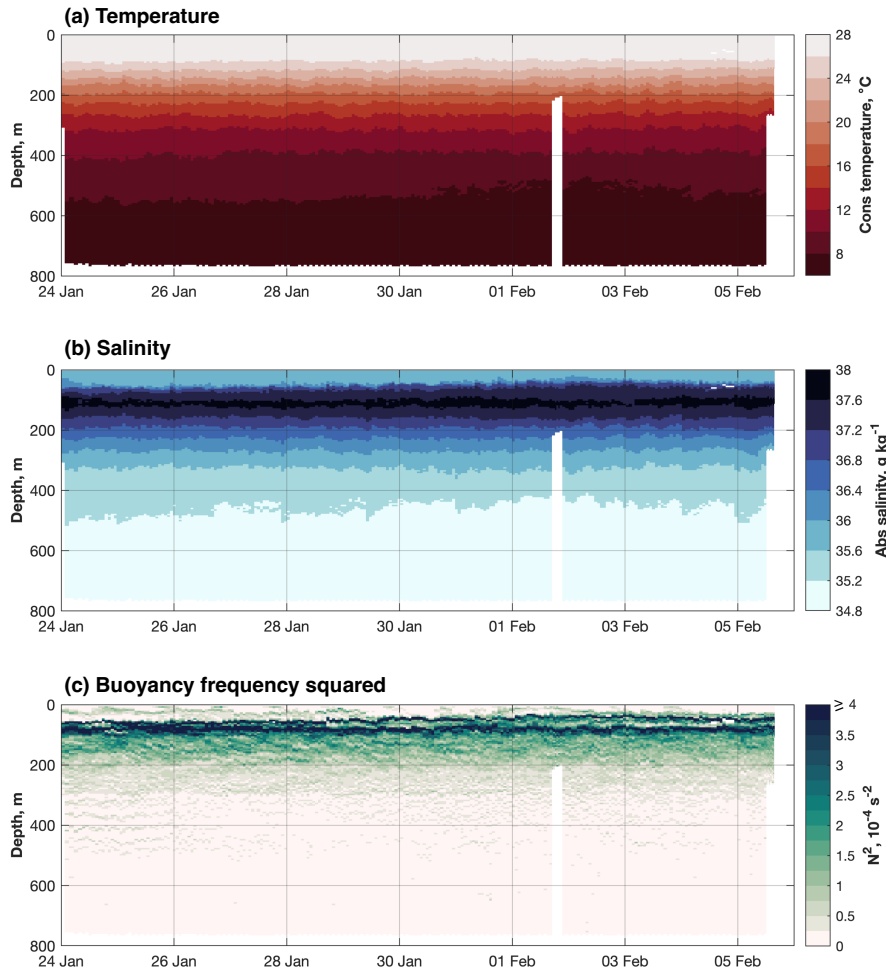
Figure 4. Time series of hydrographic observations from SG620, averaged (arithmetic mean) into 5 m bins: **(a)** conservative temperature (°C), **(b)** absolute salinity (g kg^{-1}), and **(c)** buoyancy frequency squared (N^2; s^{-2}).

Of the two estimates of ε, the higher of the two is ε_T, the geometric mean of ε_μ is 3.52 which is $3.42 \times 10^{-10 9}$ W kg^{-1}; the spatio-temporal geometric mean of ε_T is 4.96ε_μ is $3.05 \times 10^{-10 9}$ W kg^{-1}. (Each mean is calculated only from grid boxes with estimates from both methods.) The distribution of ε_T is the noisier of the two and contains higher values at depth: values of We note that, on average, the difference between the two estimates is small, and much less than an order of magnitude. The more variable of the two is ε_μ greater than 10^{-7} W kg^{-1} are not observed below 100 m (Fig. 5), whereas values of ε_T greater than 10^{-7} W kg^{-1} are on occasion observed below 100 m (Fig. 5). The greater noise in ε_T is reflected in its having a higher standard deviation , the geometric standard deviation factor (GSDF) of which is 5.58. The GSDF of ε_T is 4.43. (5.57) than ε_μ (3.94). (Note that geometric standard deviation GSDF is multiplicative, not additive.) , and is therefore dimensionless. The
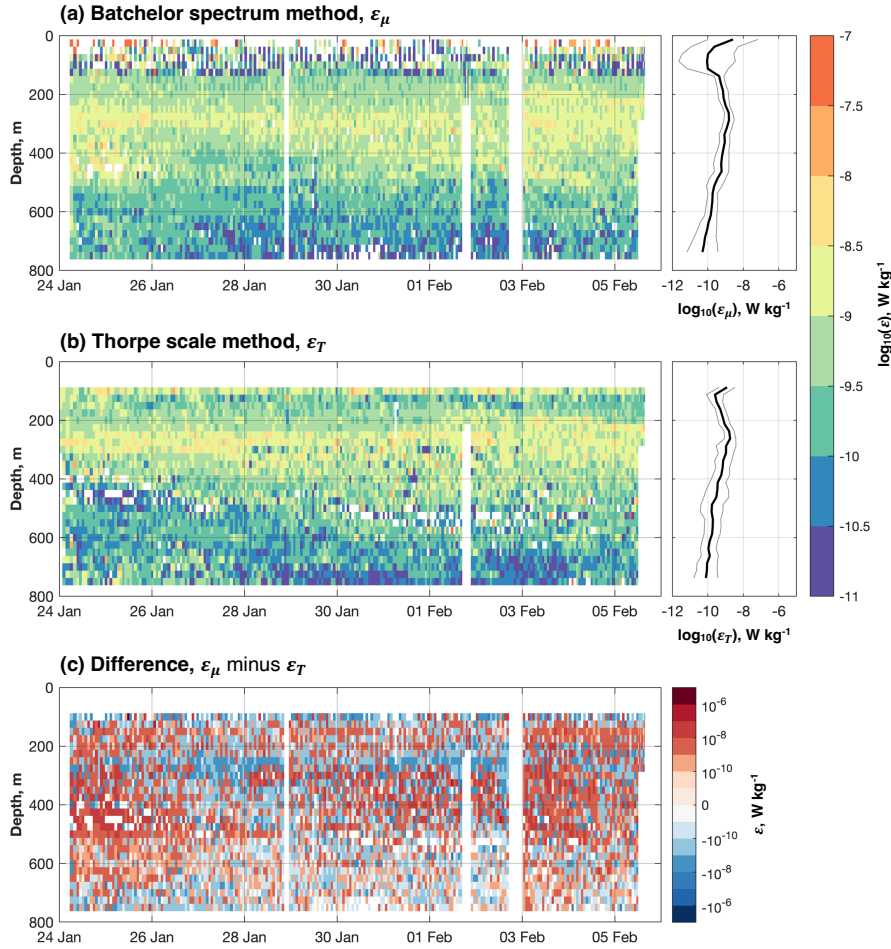
Figure 5. Turbulent kinetic energy dissipation rate, ε (W kg^{-1}) as estimated using **(a)** the Batchelor spectrum method (ε_μ) and **(b)** the Thorpe scale method (ε_T). The respective geometric means (thick lines) and geometric standard deviation factors (thin lines) are shown in the panels on the right. Note that geometric standard deviation factor is multiplicative. **(c)** The difference between ε_μ and ε_T.

range is from the $geometric\,mean/GSDF$ to $geometric\,mean \times GSDF$.) Averages and GSDFs are calculated from bins only where estimates of both ε_μ and ε_T are available.

The highest values of ε are found in approximately the top ~~100~~50 m of the water column~~(~~, in the surface mixed layer above the upper boundary of SUW ($> 10^{-8}$; Fig. 5; ε_μ only)~~, in the surface mixed layer~~. The upper boundary of SUW corresponds to the shallowest band of high buoyancy frequency (Fig. 4)~~, where ε values in excess of 10^{-7} W kg^{-1} are frequently observed. Values~~; a peak in the strength of the stratification might be expected to arrest the downward penetration of surface mixing. But these highest values are infrequently observed: a large proportion of ε_μ ~~as low as~~ estimates in the mixed layer are greater than 2×10~~$^{-11}$ W kg^{-1} are also observed in the surface mixed layer~~, albeit less frequently. Hence,

the mean -7, beyond the range for which the FP07 fast thermistor observations and the Batchelor spectrum method yield meaningful results (Sec. 2.2; Peterson and Fer, 2014). Consequently, the remaining values are all below this threshold; indeed, considerable variability in ε_μ in the upper water column (< is observed in the mixed layer – this is reflected in the relatively high GSDF for ε_μ in this region (Fig. 5) – and many remaining estimates are low (< 10^{-9} W kg^{-1}) is larger than at other depths, but the standard deviation (approximately 10^{-2} W kg^{-1} 10) is also larger than at other depths. The mean ε_μ in the upper water column is therefore likely to be biased towards these low values. In the remainder of the water column, ε_μ and ε_T are predominantly below 2×10^{-7} (Fig. 5; right-hand panels)), hence the comparison between the two is meaningful.

Immediately below the high-ε surface mixed layer

Between approximately 100 and 200 m, a thin layer of relatively low with moderate values of ε lies within SUW in the upper thermocline, between approximately 100 and 200 m (Figs. 4 and 5). Here, values of both ε_μ and ε_T are commonly between $10^{-9.5}$ and 10^{-9} W kg^{-1}. This low-ε layer is clearly seen in the mean profiles (Fig. 5). Below the upper boundary of SUW, found between at 50 to 75 m, highest values of ε are less frequently observed (Figs. 5 and 4). The upper boundary corresponds to the shallowest band of high buoyancy frequency (Fig. 4); a peak in the strength of the stratification that might be expected to arrest the downward penetration of surface mixing.

Below this low-ε SUW layer, between approximately 200 and 500 m, is a relatively thick layer with higher values of ε ($10^{-9} < \varepsilon < 10^{-8}$ W kg^{-1}; Fig. 5). Values of ε_T in this layer are generally higher than values of ε_μ (Fig. 5), which would explain why the distribution of ε_μ ε_T is slightly skewed to lower values, while higher values than the distribution of ε_T is slightly skewed to higher values ε_μ (Fig. ??6a). A few values of ε_T are in excess of $10^{-7.5}$ W kg^{-1} (Fig. 5). These high values are typically those in the modest secondary peak in the distribution of ε_T between 10^{-6} and 10^{-5} W kg^{-1} (Fig. ??). The thickness of this higher-ε_μ and -ε_T layer increases by 50 to 100 m over the course of the deployment. Below 700 m, both ε_μ and ε_T are less than 10^{-10} W kg^{-1} between 28 January and 4 February; the differences between the two estimates also tend to be lower within this spatio-temporal range (Fig. 5c). This is in contrast to higher values of ε_μ and ε_T (< > 10^{-11} 10 W kg^{-1}) within the 700 to 800 m depth range at the beginning and end of the deployment.

3.2 Heat and salt fluxes

We use the Osborn relation to calculate diapycnal diffusivity, κ_ρ (m^2 s^{-1}), from ε using the Osborn relation:

$$\kappa_\rho = \Gamma \frac{\varepsilon}{N^2} \qquad (7)$$

where Γ is mixing efficiency, which is here taken to be 0.2 (Osborn, 1980). We use ε_μ in preference to ε_T because ε_μ the former has better coverage in the mixed layer (Fig. 5).

The Below approximately 250 m, the distribution of κ_ρ resembles that of ε_μ, notwithstanding a decrease in due to the relatively low variability in N^2 at these depths (Fig. 4c). Above 200 m, N^2 increases substantially in the pycnocline and thus κ_ρ at mid-depth between the 26 and 28 January where ε_μ remains relatively high (Figs. 5a and 7a). Excluding decreases. Beneath
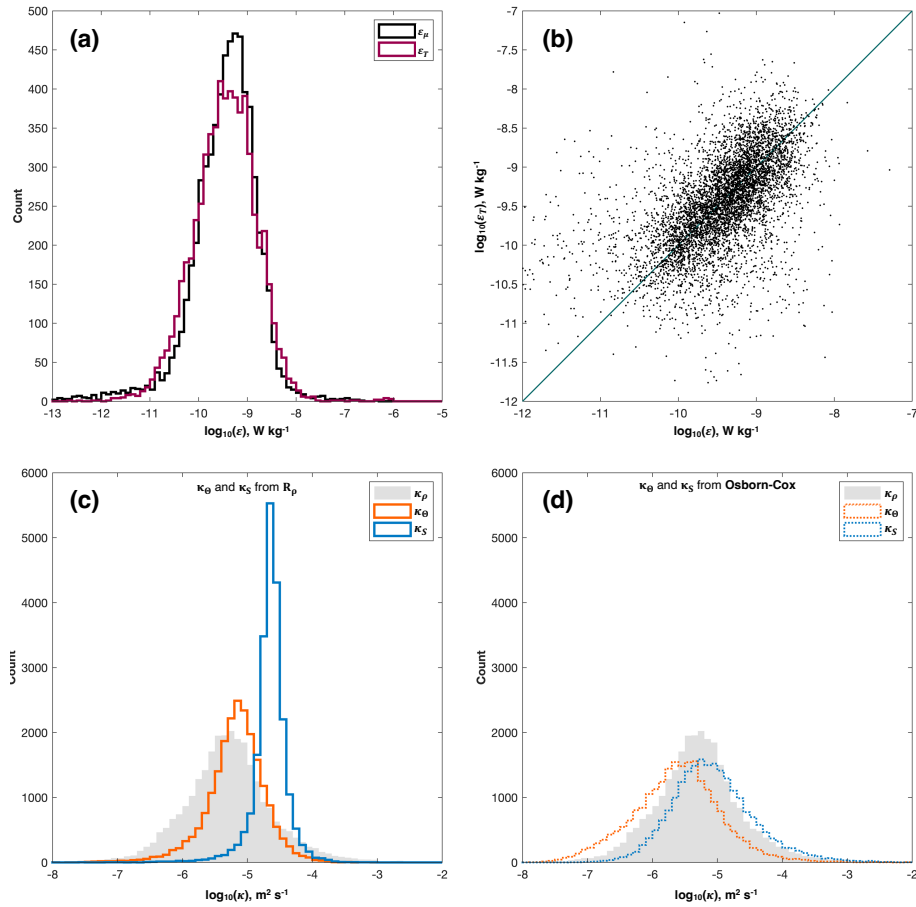
Figure 6. (a) Histograms of turbulent kinetic energy dissipation rate as estimated using the Batchelor spectrum method (ε_μ; green line) and the Thorpe scale method (ε_T; purple line; both W kg^{-1}). **(b)** Scatter plot of ε_T against ε_μ. The one-to-one line is shown in dark green. **(c)** Histograms of thermal diffusivity (κ_Θ; orange line) and haline diffusivity (κ_S; blue line) as estimated from the density ratio, R_ρ. Diffusivity, κ_ρ, estimated from the Osborn relation and ε_μ is plotted as the shaded grey histogram. **(d)** Histograms of κ_Θ (orange dotted line) and κ_S (blue dotted line) as estimated from χ using the Osborn-Cox relation. Diffusivity estimated from the Osborn relation is plotted as the shaded grey histogram, as in (c).

the surface mixed layer, κ_ρ is highest between 400 and 500 m ($< 10^{-4.5}$ m^2 s^{-1}; Fig. 7a), with low values predominating in the core of the high-salinity SUW ($< 10^{-6}$ m^2 s^{-1}; Fig. 7a).

Vertical turbulent heat and salt fluxes, Q_h (W m^{-2}) and Q_S (kg m^{-2} s^{-1}) respectively, can be calculated from κ_ρ:

$$Q_h = -\rho C_p \kappa_\rho \Theta_z \tag{8}$$
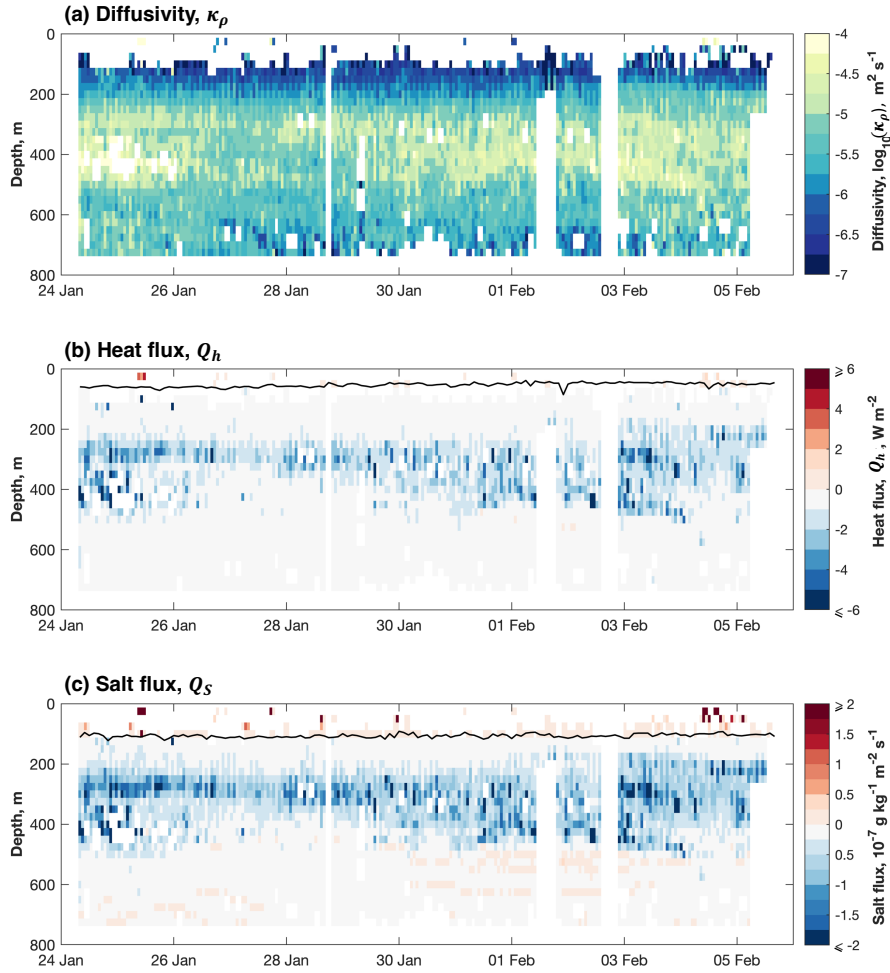
Figure 7. **(a)** Diffusivity, $log_{10}(\kappa_\rho)$ (m² s⁻¹). **(b)** Vertical heat flux, Q_h (W m⁻²). **(c)** Vertical salt flux, Q_S (10⁻⁷ g kg⁻¹ m⁻² s⁻¹). Negative fluxes are downward. All are calculated from ε calculated using the Batchelor spectrum method. The black lines in panels (b) and (c) indicate the depth of, respectively, the temperature and salinity maxima, as derived from 1 m binned Seaglider observations.

$$Q_S = \frac{1}{1000}(-\rho\kappa_\rho S_z) \qquad (9)$$

where ρ is density, C_p is the specific heat capacity of seawater, Θ_z is the vertical gradient of conservative temperature, and S_z is the vertical gradient of absolute salinity.

Beneath the surface mixed layer, both Q_h and Q_S are predominantly negative (i.e. downward) because temperature and salinity decrease with depth (Fig. 4a and b). The most prominent feature of the distributions of both is the broad region of negative (i.e. downward) turbulent heat and salt transport between approximately 200 and 500 m (Fig. 7b and c). This

corresponds to the elevated values of ε ($> 10^{-5}$ W kg^{-1}) found within same depth range (Fig. 7a). Within the surface mixed layer, notwithstanding the limited coverage of the observations, Q_h is positive in the top 50 m and negative between 50 and 100 m; ~~by contrast,~~ Q_S is positive throughout the surface mixed layer (Fig. 7b and c). This is due to weak thermal and haline inversions near the surface; the depths of the temperature and salinity maxima are indicated by the black lines in Fig. 7b and c respectively.

~~(a) Diffusivity, $log_{10}(\kappa_\rho)$ (m^2 s^{-1}). (b) Vertical heat flux, Q_h (W m^{-2}). (c) Vertical salt flux, Q_S (10^{-7} g kg^{-1} m^{-2} s^{-1}). Negative fluxes are downward. All are calculated from ε calculated using the Batchelor spectrum method.~~

~~(a) Thermal diffusivity, κ_Θ and (b) haline diffusivity, κ_S (both m^2 s^{-1}), in the presence of double-diffusive convection. Both diffusivities are plotted only in gradient layers of thermohaline staircases.~~

We now focus on the 200 to 500 m depth range, the region of highest κ_ρ and, consequently, the region in which Q_h and Q_S are most pronounced. Over the period of the observations, the arithmetic mean Q_h between 200 and 500 m was $-$~~1.45~~1.40 W m^{-2}~~; integrated over a year, this results in an annual turbulent heat flux of -4.58×10^7 J m^{-2}. Over the period of the observations, the~~. This, and all subsequent flux estimates, are summarised in Table 1. The arithmetic mean Q_S between 200 and 500 m was $-$~~6.03~~5.84 $\times 10^{-8}$ kg m^{-2} s^{-1}~~; integrated over a year, this results in an annual turbulent salt flux of -1.90 kg m^{-2}.~~

~~These fluxes, being derived from ε, represent transports of heat and salt that are driven by turbulent, mechanical mixing.~~ This is a relatively low-turbulence region~~, and the~~; the attendant turbulent fluxes are correspondingly relatively small and likely have little influence on the region's hydrography. For instance, ~~we estimate that the annually integrated turbulent fluxes~~ integrated over a year, Q_h results in an annual turbulent heat flux of -4.43×10^7 J m^{-2}, which would reduce the temperature ~~and salinity~~ of the overlying SUW layer (assumed to be 100 m thick) by just 0.11°C~~and~~. Similarly integrated over a year, Q_S results in an annual turbulent salt flux of -1.84 kg m^{-2}, which would reduce the salinity of the overlying SUW layer by just 0.02 g kg^{-1}~~respectively.~~.

3.3 Salt fingers and associated fluxes

Diffusivity as estimated using the Osborn relation, κ_ρ (Eqn. 7) and the associated fluxes presented above are derived from ε, and so are applicable to transports of heat and salt that are driven by turbulent, mechanical mixing (turbulent regime). However, these ε-based estimates do not account for the fluxes driven by the salt fingers (i.e. double-diffusive mixing; salt-finger regime) that are characteristic of the thermohaline staircases ~~that are~~ prominent in the western tropical Atlantic (Schmitt et al., 1987; Rollo et al., 2022); Seaglider 620 was deployed at the edge of the region identified by Schmitt et al. (1987) as being the location of strong staircase structures. ~~In~~ Such structures are prominent in the temperature observations (Fig. 8). In the turbulent regime, thermal diffusivity, κ_Θ and haline diffusivity, κ_S, are the same. But in the salt finger regime, κ_S may be approximately twice κ_Θ, hence they shall hereafter be considered separately. Moreover, in low-turbulence ~~regimes, double-diffusive mixing gives~~ regions, such as that of the present study, salt fingers give rise to fluxes of heat and salt that can be larger than those driven by mechanical turbulence (Schmitt, 1988).
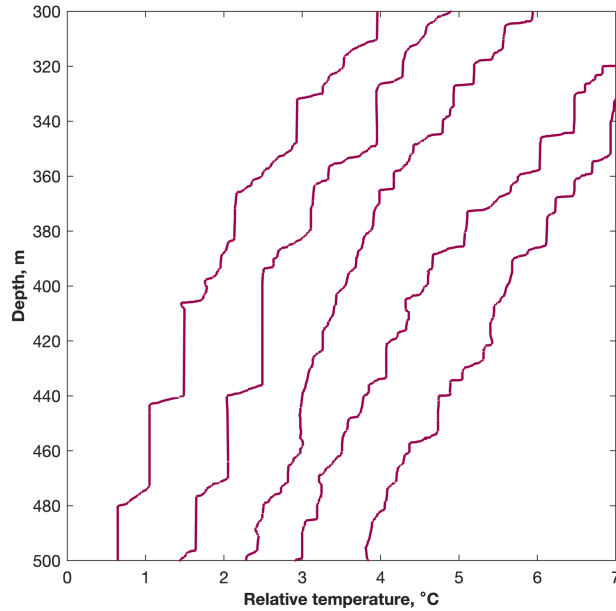
Figure 8. A selection of temperature profiles (presented as relative conservative temperature, °C) recorded by the FP07 fast thermistor. Thermohaline staircases are visible at a variety of scales.

3.4 ~~Double diffusion and associated fluxes~~

325 ~~We use the algorithm of Rollo et al. (2022) to identify gradient layers in thermohaline staircases: that is, regions of likely active salt fingering in which double diffusive convection occurs. The algorithm identifies both mixed-layers and the gradient-layers between them at 1 m resolution~~Those regions of the water column that are susceptible to salt fingers may be identified using the Turner angle, Tu: salt fingers can occur where $45° < Tu < 90°$. The following equations are applied only where this condition is met. Tu is calculated from temperature and salinity binned into 5 m vertical bins; all subsequent diffusivities are calculated 330 from variables binned into 5 m vertical bins in order to match Tu.

~~To estimate haline diffusivity,~~

We compare two different estimates of κ_Θ and κ_S ~~, in the presence of salt fingering~~in the salt finger regime. Firstly, and given that theoretical flux laws can overestimate κ_S in the real ocean (e.g. Taylor and Veronis, 1996; Kelley et al., 2003; Radko, 2005), we follow van der Boog et al. (2021) in using the ~~empirically determined~~empirical relations of Radko and Smith (2012)~~:~~

335
$$\kappa_S = \left(\frac{135}{(R_\rho - 1)^{1/2}} - 62.75 \right) K R_\rho$$
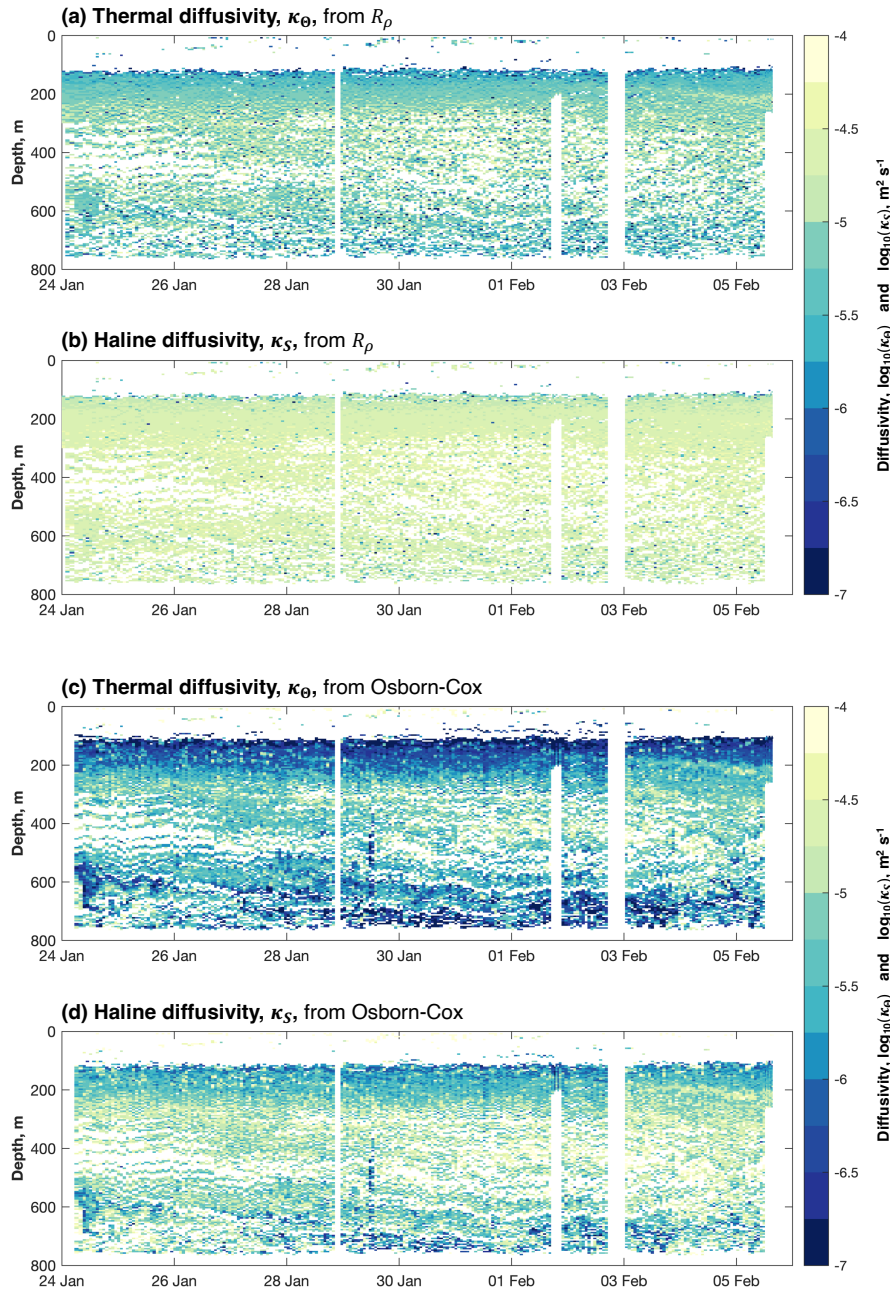
Figure 9. **(a)** Thermal diffusivity, κ_Θ and **(b)** haline diffusivity, κ_S (both $m^2\ s^{-1}$), in the presence of salt fingers as calculated from the density ratio, R_ρ, and the molecular diffusivity of heat, K following van der Boog et al. (2021). **(c)** κ_Θ and **(d)** κ_S in the presence of salt fingers as calculated from our estimates of χ using the Osborn-Cox relation (Sec. 2.2; Osborn and Cox, 1972). Diffusivities are plotted only in regions of the water column susceptible to salt fingers, i.e. where the Turner angle is between 45 and 90°.

where $R_\rho = \alpha\Theta_z/\beta S_z$ is to calculate κ_Θ and κ_S from the density ratio, α is the thermal expansion co-efficient, β is the haline contraction coefficient, and K is R_ρ (Eqn. 6), and the molecular diffusivity of heat., K, estimated from temperature and salinity at each grid point:

$$\kappa_S = \left(\frac{135}{(R_\rho - 1)^{1/2}} - 62.75 \right) K R_\rho \tag{10}$$

340 From κ_S, also again following van der Boog et al. (2021) and Radko and Smith (2012), we then calculate κ_T κ_Θ:

$$\kappa_\Theta = \kappa_S \frac{\gamma}{R_\rho} \tag{11}$$

where $\gamma = 2.709 e^{-2.513 R_\rho} + 0.5128$ is the density flux ratio in the presence of salt fingers. We refer to these salt finger diffusivities as κ_Θ and κ_S from R_ρ (Figure 9a and b).

Thermal diffusivity in the presence of double diffusion is similar to that caused by mechanical turbulence Secondly, we use

345 the Osborn and Cox (1972) relation to estimate κ_Θ and κ_S using χ (Eqn. 2; see also e.g. St Laurent and Schmitt, 1999; Schmitt et al., 2005), which we calculated as an intermediary step in the calculation of ε_μ (Sec. 2.2):

$$\kappa_\Theta = \frac{\chi}{2\Theta_z^2} \tag{12}$$

The relationship between κ_Θ and κ_S when calculated from χ remains as in Eqn. 11 (Schmitt et al., 2005; van der Boog et al., 2021). We refer to these second salt finger diffusivities as Osborn-Cox κ_Θ and κ_S.

350 There is approximately an order of magnitude difference between κ_Θ and κ_S from R_ρ, the latter being the greater (Figs. 7 6c, and 9a and ??a); haline diffusivity is higher b). Neither distribution exhibits the same pronounced structure as κ_ρ (Fig. 7a): whereas κ_ρ resembles the distribution of ε_μ from which is was derived (Fig. 5a) – i.e. with elevated values between 200 and 500 m, and lower values below and, in particular, immediately above – values of κ_Θ and κ_S from R_ρ are relatively constant in depth and time. Of the two, κ_S is the larger, being generally greater than $10^{-4.5}$ m^2 s^{-1}; κ_Θ is generally between 10^{-6} and

355 10^{-5} m^2 s^{-1}, although some values higher than this are present (Figs. 7a 6c, and 9a and b). Estimates of both κ_Θ and ??b). The mean κ_S from R_ρ are higher than estimates of κ_ρ at the same depth (Figs. 7a, and 9a and b), indicating that the vertical mixing of properties in the salt-finger regime is higher than in the turbulent regime.

We then substitute κ_Θ from R_ρ (Fig. 9a) into Eqn. 8 in place of κ_ρ (Fig. 7a). Averaged (arithmetic mean) between 200 and 500 m is 1.13, κ_Θ from R_ρ gives rise to a heat flux of -1.71 W m^{-2} in the salt-finger regime (Table 1), an annual temperature

360 reduction of 0.13°C in the SUW layer. This flux is larger than the value reported above for the turbulent regime (Sec. 3.2). Similarly, we substitute κ_S from R_ρ (Fig. 9b) into Eqn. 9 in place of κ_ρ. Averaged (arithmetic mean) between 200 and 500 m, κ_S from R_ρ gives rise to a salt flux of -1.83×10^{-5} ^{7} mkg m^{-2} s^{-1}, the mean of κ_T is 1.44 × in the salt-finger regime (Table 1), or an annual reduction of 0.06 g kg^{-1} in the salinity of the SUQ layer. This flux is over three times larger than the

corresponding salt flux in the turbulent regime. Note that, for the calculation of the arithmetic mean heat and salt fluxes in the salt finger regime, we set both κ_T and κ_S from R_ρ to zero outside of the salt finger regimes, i.e. where $Tu < 45°$ and $Tu > 90°$, and include these zeros in our averages. Because we first filter out regions of the water column that are not susceptible to salt fingering, gaps in the record therefore indicate an absence of the process to be averaged (i.e. salt finger-driven fluxes) rather than an absence of data.

The distributions of κ_Θ and κ_S from the Osborn-Cox relation resemble the distribution of ε, which itself resembles the distribution of χ that was used to calculate both diffusivities (not shown): the highest diffusivities are found between 200 and 500 m, with lower values being found above and below. In both cases, the highest diffusivities are between 10^{-6} and 10^{-5} m^2 s^{-1} ~~, and the mean of~~; within this range, κ_S is ~~3.12 ×~~ the greater (Figs. 6d, and 9c and d). Above and below this depth range, κ_Θ decreases to values below $10^{-\text{\st{5}}6.5}$ m^2 s^{-1} ~~. Of course, double-diffusion is spatially and temporally much more patchy than turbulent mixing, which is spatially and temporally continuous; hence, the mean values of κ_T and~~ (Fig. 9c), whereas κ_S ~~are calculated over a much smaller sample region.~~ decreases only to values of approximately $10^{-5.5}$ m^2 s^{-1} (Fig. 9c).

~~Over the period of the observations, the mean~~ ~~double-diffusive heat flux~~ We then substitute κ_Θ from the Osborn-Cox relation (Fig. 9c) into Eqn. 8 in place of κ_ρ. Averaged (arithmetic mean) between 200 and 500 m ~~was~~, ~~κ_Θ from the Osborn-Cox relation~~ gives rise to a heat flux of $-$~~5.45~~1.49 W m^{-2} ~~; integrated over a year, this results in an annual double-diffusive temperature flux of -1.72×10^8 J m^{-2}. Over the period of the observations, in~~ the ~~mean double-diffusive salt flux~~ salt-finger regime (Table 1), an annual temperature reduction of 0.11°C in the SUW layer. This heat flux is very similar to that reported for the turbulent regime, and less than that predicted by the empirical relation of Radko and Smith (2012) reported above (i.e. κ_Θ and κ_S from R_ρ). And κ_S, averaged (arithmetic mean) between 200 and 500 m ~~was~~, gives rise to a salt flux of $-$~~5.18~~9.40 $\times 10^{-\text{\st{7}}8}$ kg m^{-2} s^{-1} ~~; integrated over a year, this results in an annual double-diffusive salt flux of -16.34 kg m~~ (Table 1), an annual salinity reduction of 0.03 g kg$^{-\text{\st{2}}}$ ~~. Respectively, we estimate that these annually integrated double-diffusive fluxes would reduce the temperature and salinity of the overlying SUW layer (again assumed to be 100~~ in the SUW layer. This flux is approximately 1.6 times that reported for the turbulent regime, but half that predicted by the empirical relation of Radko and Smith (2012). As before, we set both κ_T and κ_S from the Osborn-Cox relation to zero outside of the salt finger regimes.

4 Discussion

4.1 Comparing ε_μ and ε_T

Our finding that estimates of ε_T are higher than estimates of ε_μ is in agreement with the findings of Howatt et al. (2021). They ~~conclude~~ report that, while the Thorpe scale method can well represent qualitative aspects of the spatio-temporal distribution of ε, ~~shortcomings in CTD sampling and the necessary setting of a minimum Thorpe scale, L_T (Eqn. 4)~~ the method can, when applied to relatively low resolution finescale observations, artificially inflate ε_T by an order of magnitude ~~. The~~ relative to estimates from, for instance, the Batchelor spectrum method. This is for the simple reason that finescale observations lack the resolution to capture small-scale overturns; the resultant distribution of L_T, and hence of ε is consequently biased towards high values.
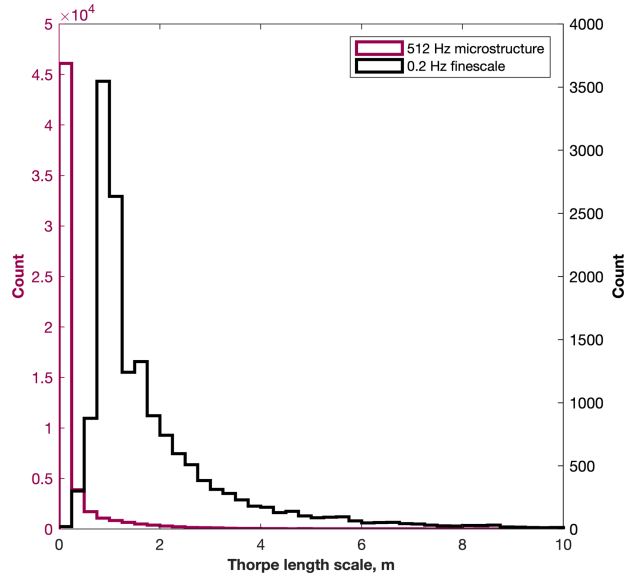
Figure 10. Histograms of Thorpe scale, L_T, as calculated from FP07 microstructure observations (green line; left-hand axis) and ordinary Seaglider finescale observations (grey line; right-hand axis).

This is supported by our observations: the differences between ε_μ and ε_T reported here are ~~not as extreme~~much lower, being, on average, far less than an order of magnitude (Sec. 3; Figs. 5 and ~~??). The very high resolution of~~ 6). Further, we directly compare L_T calculated using the FP07 ~~thermistor temperature~~ microstructure observations (512 Hz~~; approximately~~, 100 Hz when accounting for the sensor's response time; ~~Sec. 2) should reduce the minimum~~ Fig. 3) to L_T ~~compared with calculations using observations from a standard glider CT sail; however, the lack of similarly high-resolution salinity observations means that the resolution of N used to calculate ε_T in Eqn. 5 will limit any improvement that a small minimum~~ calculated using the Seaglider's ordinary finescale temperature and salinity observations (0.2 Hz). The distribution of L_T ~~might otherwise have on estimate of ε_T. Nevertheless, we estimate that the minimum~~ derived from microstructure observations has a pronounced peak at very low values ($>$ 0.25 m; Fig. 10). In contrast, the finescale glider observations are unable to resolve values of L_T ~~in the present study is 1 m; Howatt et al. (2021), who reduce the difference between their two estimates of ε, report that their minimum L_T is 2 m, so the~~ at this scale (Fig. 10). The better agreement between ε_μ and ε_T reported here ~~may~~ than by Howatt et al. (2021) therefore appears to be explained by ~~our~~ the higher vertical resolution ~~. A further limitation on using~~ of our observations. Consequently, and in agreement with Howatt et al. (2021), we suggest that, in a low-turbulence environment, the Thorpe scale method ~~to estimate~~ is unable to produce reliable quantitative estimates of ε ~~from temperature observations~~alone ~~is that any influence of salinity of density is neglected; we must assume here that density is dominated by temperature. This is a fair assumption in the tropics, especially given that , over much of~~ unless it is applied to microstructure observations. In a high-turbulence environment where overturns are large, finescale observations may be better able to accurately resolve the distribution of L_T and their relatively low resolution may not introduce such a systematic bias.

415   A potential problem with using the Thorpe scale method on Seaglider observations is the ~~upper-ocean in this region, salinity decreases with depth and thus does not dominate density.However, in regions such as the poles where salinity frequently dominates density, the Thorpe scale method applied to temperature observations along would likely not yield reliable results~~ non-vertical profile that the Seaglider collects: unlike, for instance, a ship-deployed CTD or a vertical microstructure profiler, a Seaglider follows a slanted trajectory, typically covering a horizontal distance of 4 km over a 1000 m-deep dive-climb cycle. Any resultant

420   sampling of horizontal gradients, particularly in the presence of internal waves, could artificially inflate estimates of ε_T due to false overturn detection (Thorpe, 2012). However, this is a concern only when the internal wave slope exceeds the slope of the Seaglider's trajectory. Following Howatt et al. (2021), we calculate that the mean ($\pm$ one standard deviation) of SG620's trajectory slope (from the horizontal) during the Eurec4a deployment was 0.70 ± 0.09, i.e. greater than the upper limit of the slope of internal waves (approximately 0.3; Thorpe, 1978; Howatt et al., 2021). Consequently, false overturn detection due to

425   the Seaglider's sloping trajectory is unlikely to lead to over-estimation of ε_T in this dataset.

4.2   Observed dissipation in spatial and temporal context

Values of ε in the western tropical Atlantic are broadly consistent with other open-ocean regions away from shallow topography. For instance, Sheen et al. (2013) and Naveira Garabato et al. (2016) report background ε values of approximately 10^{-10} to 10^{-9} W kg^{-1} downstream of the Drake Passage, with values in excess of 10^{-8} W kg^{-1} in the upper 1000 m and in the

430   vicinity of rough topography. George et al. (2021) report ε values between 10^{-10} to 10^{-8} W kg^{-1} in the upper layers of the southwestern Bay of Bengal. And Peterson and Fer (2014) report mission-mean values of between 10^{-8} to 10^{-7} W kg^{-1} from observations collected near the Faroe Islands in the northern Atlantic.

    Limited estimates of ε are available for the western tropical Atlantic. Two profiles from the region, collected by a microstructure turbulence profiler, were presented by Fernández-Castro et al. (2014). Similarly to our profiles, they find surface ε values

435   between approximately 10^{-7} and 10^{-6} W kg^{-1}, and values between approximately 10^{-9} and 10^{-8} W kg^{-1} between 50 and 300 m. Below 50 m, their estimates of κ_ρ are similar to ours, although they report near-surface values several orders of magnitude larger than ours (e.g. $> 10^{-3}$ m^2 s^{-1}). Our methods do not yield reliable estimates of high turbulence in the mixed layer, however, so a full comparison is not possible. Two sets of observations taken several years apart and separated by up

Table 1. Heat and salt fluxes estimates calculated using diffusivities in the turbulent and salt finger regime. Fluxes for the latter regime are estimated from R_ρ using both the empirical relations of Radko and Smith (2012), and from χ using the Osborn-Cox relation (Osborn and Cox, 1972). All flux estimates have been averaged (arithmetic mean) between 200 and 500 m.

Regime	Heat flux, Q_h (W m^{-2})	Salt flux, Q_S (kg m^{-2} s^{-1})
Turbulent	-1.40	-5.84×10^{-8}
Salt finger, R_ρ	-1.71	-1.83×10^{-7}
Salt finger, Osborn-Cox	-1.49	-9.40×10^{-8}

to hundreds of kilometres cannot be readily compared; moreover, their profiles do not extend deeper than 300 m. Interannual variability and geographic differences could be pronounced. Nevertheless, there is no evidence in their deepest observations of an increase in ε that might indicate the presence of the elevated-ε layer that we observe beneath SUW (Figs. 4 and 5) and which, to our knowledge, has not previously been described.

~~The dissipation rates~~

4.3 Diffusivity and its influence on hydrography

The distribution of κ_Θ and κ_S from the Osborn-Cox relation (i.e. from χ), resembles that of κ_ρ – itself derived from ε_μ – far more closely than do either κ_Θ and κ_S from R_ρ (Figs. 7a and 9). This is not unexpected: χ is calculated as an intermediary step in the calculation of ε_μ, and so the two variables are not wholly independent. In contrast, κ_Θ and κ_S from R_ρ have no dependency on either ε or χ. Notably, neither κ_Θ nor κ_S from R_ρ seems to be particularly influenced by features of the water column that might be expected to influence vertical diffusivity, such as stratification (Fig. 4c) or temperature and salinity gradients (not shown). Given that the Osborn-Cox relation explicitly relates diffusivity to a mixing variable (i.e. χ), we suspect that it is more accurate than the empirical relation of Radko and Smith (2012, i.e. κ_Θ and κ_S from R_ρ).

As calculated from R_ρ (Radko and Smith, 2012), heat flux due to salt fingers is 1.22 times greater than that due to turbulent mixing; as calculated from χ (Osborn and Cox, 1972), the heat flux due to salt fingers is 1.06 times that due to turbulent mixing. And as calculated from R_ρ, the salt flux due to salt fingers is 3.31 times greater that that due to turbulent mixing; as calculated from χ, the salt flux due to salt fingers is 1.6 times that due to turbulent mixing. In all instances, heat and salt fluxes due to salt fingers (i.e. double-diffusive convection) are higher than turbulent fluxes. The empirical relations of Radko and Smith (2012) predict a relatively large difference, whereas the Osborn-Cox relation predicts a difference that is relatively small – indeed, for heat, the turbulent and salt-finger fluxes are almost the same. The choice of equation used to calculate diffusivities in the salt finger regime makes a considerable difference to the result.

The dissipation rates and diffusivities presented above appear to have a limited influence on the hydrography of the study region. If the ~~dissipation estimates and resultant fluxes reported~~ turbulent fluxes estimated above are representative of annual average conditions, heat and salt from the SUW ~~later might be expected to~~ layer penetrate downwards into the ocean interior relatively slowly~~. Consequently, the temperature and salinity of SUW would be little changed by downward turbulent mixing. The downward flux of heat due to double diffusion is almost four times~~; over the 12 days of the Eurec4a Seaglider deployment, the hydrographic influence of the fluxes would be negligible. As calculated from R_ρ, the double diffusive heat flux due to salt fingers is 1.2 times greater than that due to turbulent mixing; ~~the downward flux of salt due to double diffusion is 7.5 times~~ as calculated from χ the double diffusive heat flux due to salt fingers is the same as that due to turbulent mixing. ~~Nevertheless, integrated over a year, these fluxes are still relatively small. The properties of SUW are likely little influenced by the downward mixing of heat and salt into the ocean interior.~~ Salt fingers potentially have a greater influence on hydrography that turbulent mixing, but the overall effect would still be near inconsequential.

5 Conclusions

We demonstrate that microstructure temperature observations collected by a Seaglider-mounted FP07 fast thermistor may be used to estimate the dissipation rate of turbulent kinetic energy, ε. We estimate ε using the Batchelor spectrum method (ε_μ) and the Thorpe scale method (ε_T). The results from the two methods agree well, although ε_T is on average higher than ε_μ. This is in agreement with previous studies, although the difference reported here, which is less than an order of magnitude, is below that reported elsewhere. This improved agreement is due to ε_T being calculated using the same high-resolution observations as were used to calculate ε_μ: other studies (e.g. Howatt et al., 2021) have compared ε_μ to ε_T calculated using lower-resolution finescale temperature observations that are unable to resolve overturns below a certain size, thus biasing estimates of ε towards high values.

We identify a layer of elevated ε values between 200 and 500 m that lies immediately below Subtropical Underwater, a high-salinity sub-surface water mass that is co-located with a maximum in stratification. We estimate that, over the period of the deployment, this elevated ε layer is responsible for a mean heat flux of -1.40 W m^{-2} and a mean salt flux of -5.84×10^{-8} kg m^{-2} s^{-1}. Given the prevalence of double diffusion and salt fingers in the region, we estimate thermal and haline diffusivities in the salt-finger regime, and the resultant heat and salt fluxes using both the empirical relation of Radko and Smith (2012), which depends on the density ratio, R_ρ, and the relation of Osborn and Cox (1972), which depends on the rate of destruction of temperature variance, χ. Fluxes estimated using the relation of Radko and Smith (2012) are higher than those estimated using the relation of Osborn and Cox (1972). Nevertheless, turbulent and salt finger fluxes are small, and their influence on hydrography is likely limited.

Code availability. The Matlab toolbox of Scheifele et al. (2018) to calculate turbulent kinetic energy dissipation rate following the Batchelor spectrum method is available at: github.com/bscheife/turbulence_temperature.

Data availability. Standard hydrographic observations from SG620 are available from the British Oceanographic Data Centre at: doi:10/gnz8. Processed turbulent kinetic energy dissipation rate estimates, from both Batchelor and Thorpe scale methods, are available from the British Oceanographic Data Centre at: doi:10/htsw.

Author contributions. PMFS and GMD calculated turbulent kinetic energy dissipation rate following the Batchelor spectrum method. PJL calculated turbulent kinetic energy dissipation rate following the Thorpe scale method. All authors contributed to the analysis. PMFS wrote the paper with assistance from GMD and PJL, and with comments and feedback from KJH and RAH.

500 *Competing interests.* The authors declare that they have no competing interests.

Acknowledgements. PMFS, GMD, KJH and RAH were supported by the COMPASS project (grant number 741120), which was funded by the European Research Council under the Horizon 2020 programme. PJL was funded by NERC-UKRI NEXUSS PhD studentship NE/N012070/1. We thank Beth Siddle, Callum Rollo, and the crew and scientists of the RV Meteor (cruise M161) for assistance in the deployment and recovery of the glider. We thank Gareth Lee and Marcos Cobas-Garcia for the preparation of the glider, and the UEA glider

505 group for piloting. ~~We thank Callum Rollo for kindly assisting with data processing for the thermohaline staircase detection.~~

References

Batchelor, G. K.: Small-scale variation of convective quantities like temperature in a turbulence fluid. Part one: general discussion and the case of small conductivity, Journal of Fluid Mechanics, 5, 113 133, 1959.

Creed, E., Ross, W., Lueck, R., Stern, P., Douglas, W., Wolk, F., and Hall: Integration of an RSI microstructure sensing package into a Seaglider, Oceans 2015 – MTS/IEEE Washington, 2015.

Dillon, T. M.: Vertical overturns: A comparison of Thorpe and Ozmidov scales, Journal of Geophysical Research, 87, 9601 – 9631, 1982.

Fer, I., Nandi, P., Holbrook, W. S., Schmitt, R. W., and Páramo, P.: Seismic imaging of a thermohaline staircase in the western tropical North Atlantic, Ocean Science, 6, 621 – 631, 2010a.

Fer, I., Skogseth, R., and Geyer, F.: Internal waves and mixing in the marginal ice zone near the Yermak Platuea, Journal of Physical Oceanography, 40, 1613 – 1630, 2010b.

Fer, I., Peterson, A. K., and Ullgren, J. E.: Microstructure measurements from an underwater glider in the turbulent Fareo Bank Channel overflow, Journal of Atmospheric and Oceanic Technology, 31, 1128 – 1150, 2014.

Fernández-Castro, B., Mouriño-Carballido, B., Benítez-Barrios, V. M., Chouciño, P., Fraile-Nuez, E., Graña, R., Piedeleu, M., and Rodríguez-Santana, A.: Micostructure turbulence and diffusivity parameterisation in the tropical and subtropical Atlantic, Pacific and Indian Oceans during the Malaspina 2010 expedition, Deep-Sea Research I, 94, 15 – 30, 2014.

Frajka-Williams, E., Eriksen, C. C., Rhines, P. B., and Harcourt, R. R.: Determining vertical water velocities from Seaglider, Journal of Atmospheric and Oceanic Technology, 28, 1641 – 1656, 2011.

Frajka-Williams, E., Brearley, J. A., Nash, J. D., and Whalen, C. B.: New technological frontiers in ocean mixing, in: Ocean mixing: drivers, mechanisms and impacts, edited by Meredith, M. P. and Naveira Garabato, A. C., Elsevier Science, Amsterdam, The Netherlands, 2021.

Garau, B., Ruiz, S., Zhang, W. G., Pascual, A., Heslop, E., Kerfoot, J., and Tintoré, J.: Thermal lag correction on Slocum CTD glider data, Journal of Atmospheric and Oceanic Technology, 28, 1065 – 1071, 2011.

George, J. V., Vinayachandran, P. N., and Nayak, A. A.: Enhanced double-diffusive salt flux from the high-salinity core of Arabian Sea-origin waters to the Bay of Bengal, Journal of Physical Oceanography, 51, 505 – 518, 2021.

Howatt, T., Waterman, S., and Ross, T.: On using the finescale parameterisation and Thorpe scales to estimate turbulence from glider data, Journal of Atmospheric and Oceanic Technology, 38, 1187 – 1204, 2021.

Ijichi, T. and Hibiya, T.: Observed variations in turbulent mixing efficiency in the deep ocean, Journal of Physical Oceanography, 48, 1815 – 1830, 2018.

Kelley, D. E., Fernando, H. J. S., Gargett, A. E., Tanny, J., and Özsoy, E.: The diffusive regime of double-diffusive convection, Progress in Oceanography, 56, 461 – 481, 2003.

Lueck, R. G., Wolk, F., and Yamazaki, H.: Oceanic velocity microstructure measurements in the 20th century, Journal of Oceanography, 58, 153 – 174, 2002.

Mater, B. D., Venayagamoorthy, S. K., St Laurent, L., and Moum, J. N.: Biases in Thorpe-scale estimates of turbulence dissipation. Part 1: assessments from large-scale overturns in oceanographic data, Journal of Physical Oceanography, 45, 2497 – 2521, 2015.

Naveira Garabato, A. C., Polzin, K. L., Ferrari, R., Zika, J. D., and Forryan, A.: A microscale view of mixing and overturning across the Antarctic Circumpolar Current, Journal of Physical Oceanography, 46, 233 – 254, 2016.

Oakey, N. S.: Determination of the rate of dissipation of turbulent energy from simultaneous temperature and velocity shear microstructure measurements, Journal of Physical Oceanography, 12, 256 – 271, 1982.

Osborn, T. R.: Estimates of the local rate of vertical diffusion from dissipation measurements, Journal of Physical Oceanography, 10, 83 – 89, 1980.

545 Osborn, T. R. and Cox, C. S.: Oceanic fine structure, Geophysical Fluid Dynamics, 3, 321 – 345, 1972.

Ozmidov, R. V.: On the turbulent exchange in a stably stratified ocean, Atmospheric and Oceanic Physics, 8, 853 – 860, 1965.

Palmer, M. R., Stephenson, G. R., Inall, M. E., Balfour, C., Düsterhus, A., and Green, J. A. M.: Turbulence and mixing by internal waves in the Celtic Sea determined from ocean glider microstructure measurements, Journal of Marine Systems, 144, 57 – 69, 2015.

Peterson, A. K. and Fer, I.: Dissipation measurements using temperature microstructure from an underwater glider, Methods in Oceanogra-
550 phy, 10, 44 – 69, 2014.

Polzin, K. L., Naveira Garabato, A. C., Huussen, T. N., Sloyan, B. M., and Waterman, S.: Finescale parameterizations of turbulent dissipation, Journal of Geophysical Research: Oceans, 119, 1383 – 1419, 2014.

Radko, T.: What determines the thickness of layers in a thermohaline staircase?, Journal of Fluid Mechanics, 523, 79 – 98, 2005.

Radko, T. and Smith, P. D.: Equilibrium transport in double-diffusive convection, Journal of Fluid Mechanics, 690, 5 – 27, 2012.

555 Rainville, L., Gobat, J. L., Lee, C. M., and Shilling, G. B.: Multi-month dissipation estimates using microstructure from autonomous under-
water gliders. Multi-month dissipation estimates using microstructure from autonomous underwater gliders., Oceanography, 30, 49 – 50, 2017.

Rollo, C., Heywood, K. J., and Hall, R. A.: Glider observations of thermohaline staircases in the tropical North Atlantic using an automated classifier, Geoscientific Instrumentation, Methods and Data Systems, 11, 359 – 373, 2022.

560 Ruddick, B., Anis, A., and Thompson, K.: Maximum likelihood spectral fitting: the Batchelor spectrum, Journal of Atmospheric and Oceanic Technology, 17, 1541 – 1555, 2000.

Scheifele, B., Waterman, S., Merckelbach, L., and Carpenter, J. R.: Measuring the dissipation rate of turbulence kinetic energy in strongly stratified, low-energy environments: a case study from the Arctic Ocean, Journal of Geophysical Research: Oceans, 123, 5459 – 5480, 2018.

565 Schmitt, R. W.: Mixing in a thermohaline staircase, in: Small-scale turbulence and mixing in the ocean: proceedings of the 19th International Liège Colloquium on ocean hydrodynamics, edited by Nihoul, J. C. J. and Jamart, B. M., pp. 435 – 452, Elsevier, Amsterdam, The Netherlands, 1988.

Schmitt, R. W., Perkins, H., Boyd, J. D., and Stalcup, M. C.: C-SALT: an investigation of the thermohaline staircase in the western tropical North Atlantic, Deep-Sea Research, 34, 1655 – 1665, 1987.

570 Schmitt, R. W., Ledwell, J. R., Montgomery, E. T., Polzin, K. L., and Toole, J. M.: Enhanced diapycnal mixing by salt fingers in the thermocline of the tropical Atlantic, Science, 308, 685 – 688, 2005.

Schultze, L. K. P., Merckelbach, L. M., and Carpenter, J. R.: Turbulence and mixing in a shallow shelf sea from underwater gliders, Journal of Geophysical Research: Oceans, 122, 9029 – 9109, 2017.

Scott, R. M., Brearley, J. A., Naveira Garabato, A. C., Venables, H. J., and Meredith, M. P.: Rates and mechanisms of turbulent mixing in a
575 coastal embayment of the West Antarctic Peninsula, Journal of Geophysical Research: Oceans, 126, e2020JC016 861, 2021.

Sheen, K. L., Brearley, J. A., Naveira Garabato, A. C., Smeed, D. A., Waterman, S., Ledwell, J. R., Meredith, M. P., St Laurent, L., Thurnherr, A. M., Toole, J. M., and Watson, A. J.: Rates and mechanisms of turbulent dissipation and mixing in the Southern Ocean: results from the Diapycnal and Isopycnal Mixing Experiment in the Southern Ocean (DIMES), Journal of Geophysical Research: Oceans, 118, 2774 – 2792, 2013.

580 Smyth, W. D., Moum, J. N., and Caldwell, D. R.: The efficiency of mixing in turbulent patches: inferences from direct simulations and microstructure observations, Journal of Physical Oceanography, 31, 1969 – 1992, 2001.

Sommer, T., Carpenter, J. R., Schmid, M., Lueck, R. G., and A., W.: Revisiting microstructure sensor responses with implications or double-diffusive fluxes, Journal of Atmospheric and Oceanic Technology, 30, 1907 – 1923, 2013.

St Laurent, L. and Schmitt, R. W.: The contribution of salt fingers to vertical mixing in the North Atlantic Tracer Release Experiment, Journal 585 of Physical Oceanography, 29, 1404 – 1424, 1999.

Stevens, B., Bony, S., Farrell, D., Ament, F., Blyth, A., Fairall, C., Karstensen, J., Quinn, P. K., et al.: EUREC4A, Earth System Science Data, 13, 4067 – 4119, 2021.

Taylor, J. R. and Veronis, G.: Experiments on double-diffusive sugar-salt fingers at high stability ratio, Journal of Fluid Mechanics, 321, 315 – 333, 1996.

590 Thorpe, S. A.: Turbulence and mixing in a Scottish loch, Philosophical Transactions of the Royal Society of London, 286A, 125 – 181, 1977.

Thorpe, S. A.: On the shape and breaking of finite amplitude internal gravity waves in a shear flow, Journal of Fluid Mechanics, 85, 7 – 31, 1978.

Thorpe, S. A.: Measuring overturns with gliders, Journal of Marine Research, 70, 93 – 117, 2012.

van der Boog, C. G., Dijkstra, H. A., Pietrzak, J. D., and Katsman, C. A.: Double-diffusive mixing makes small contribution to the global 595 ocean circulation, Nature Communications Earth & Environment, 2, 46, 2021.

Whalen, C. B.: Best practices for comparing ocean turbulence measurements across spatiotemporal scales, Journal of Atmospheric and Oceanic Technology, 38, 837 – 841, 2021.

Whalen, C. B., Talley, L. D., and MacKinnon, J. A.: Spatial and temporal variability of global ocean mixing inferred from Argo profiles, Geophysical Research Letters, 39, L18 612, 2012.

600 Whalen, C. B., MacKinnon, J. A., Talley, L. D., and Waterhouse, A. F.: Estimating the mean diapycnal mixing using a finescale parameterisation, Journal of Physical Oceanography, 45, 1174 – 1188, 2015.